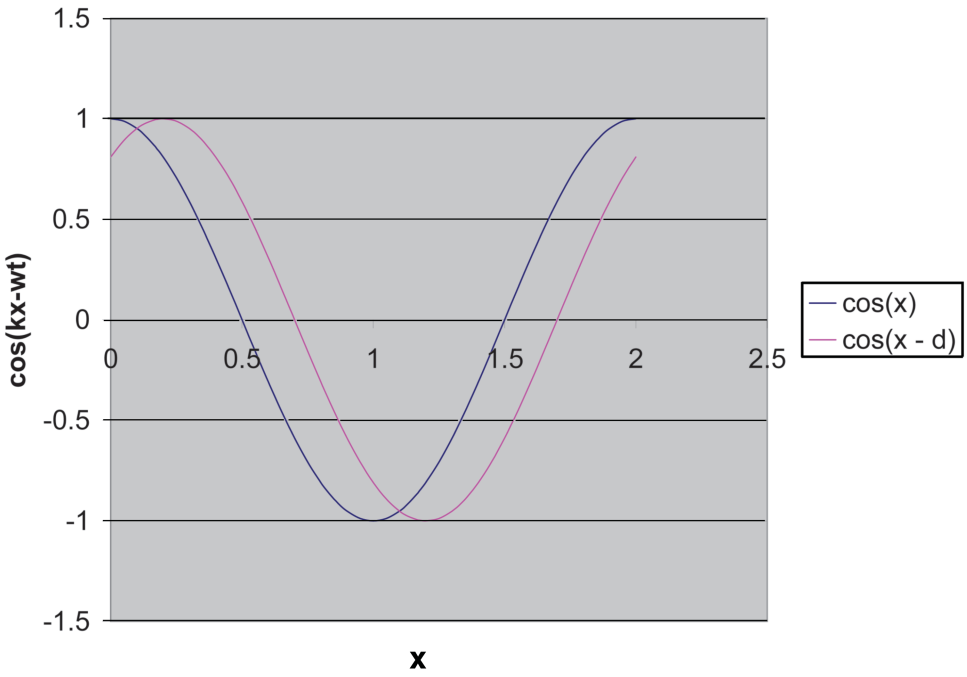

Figure 2.1. An oscillating function with argument (*kx* – *wt*) moves to the right as time advances.

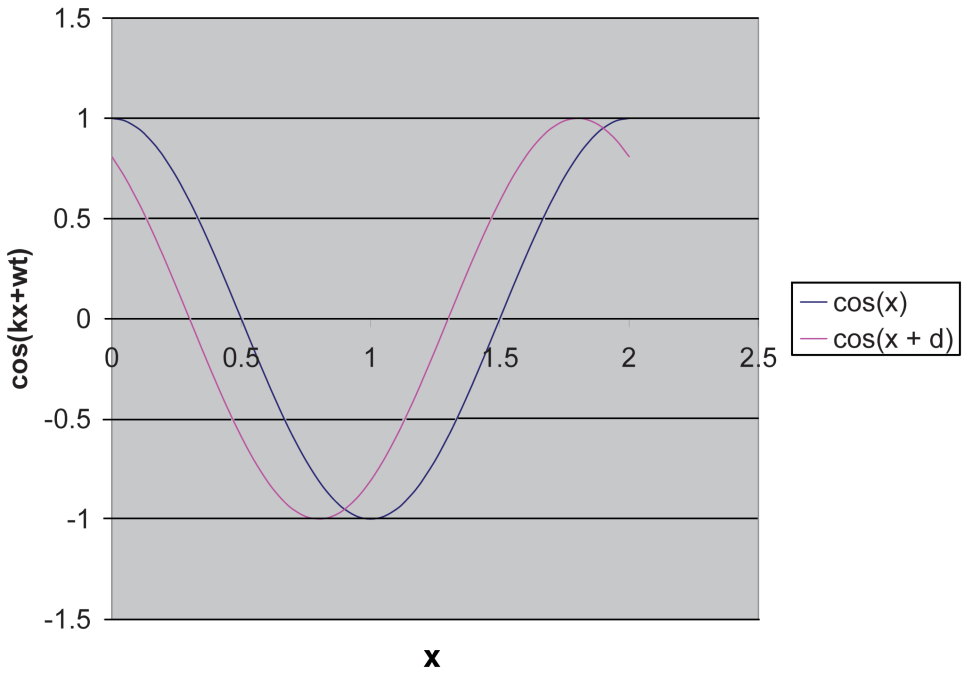

Figure 2.2. An oscillating function with argument ($kx + wt$) moves to the left as time advances.

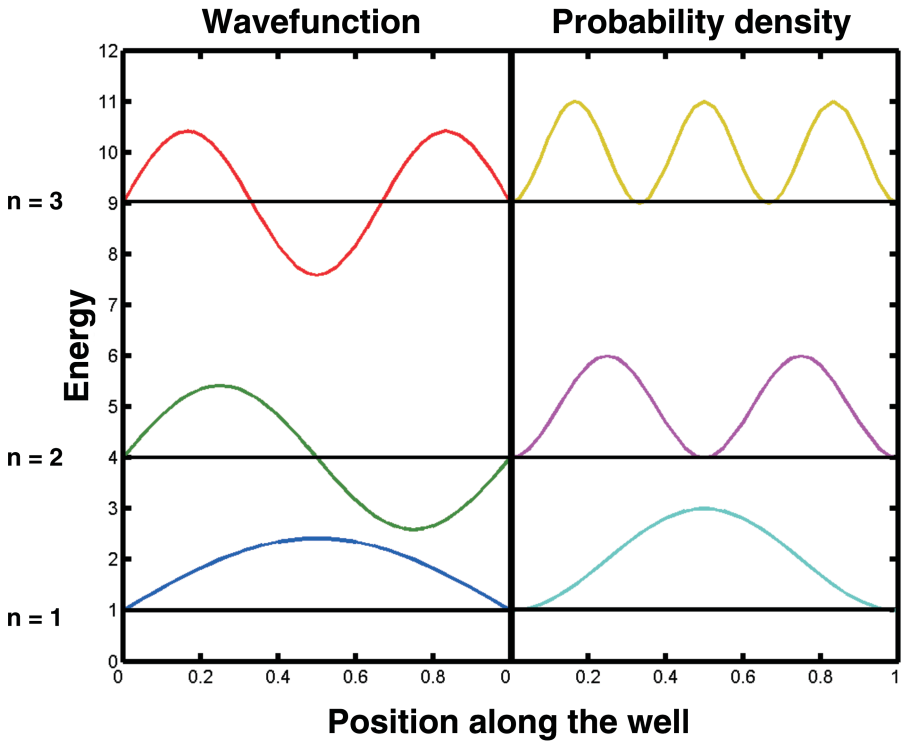

Figure 2.3. The first three solutions to the Schrödinger equation for the one-dimensional particle-in-a-well problem are displayed placed at their respective energies in the well.

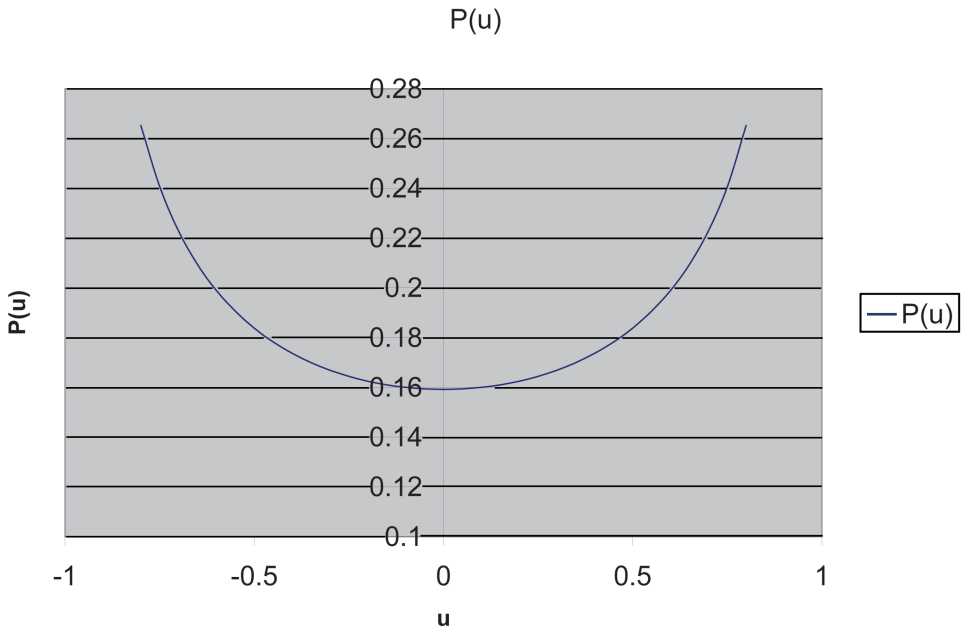

Figure 2.4. The probability of locating a particle executing classical harmonic oscillator motion measured along its trajectory.

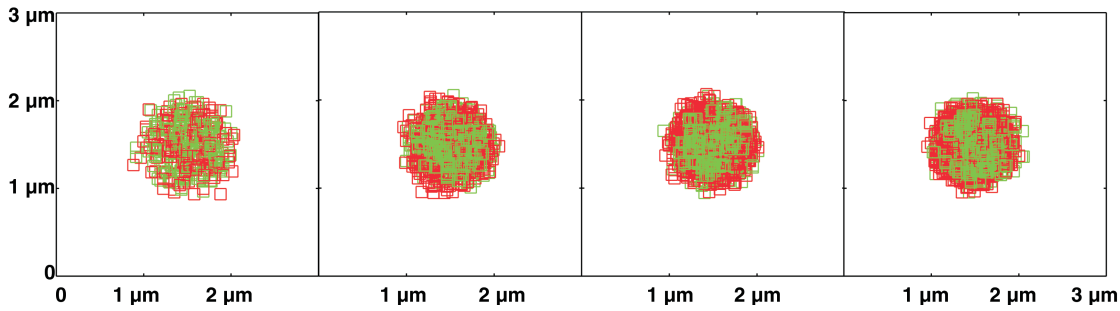

Figure 3.4. Effect of receptor–ligand complex diffusivity, $P_{\mathrm{diff}(C)}$, on B cell immune synapse formation. BCR/antigen complexes are shown in green, whereas adhesive LFA-1/ICAM-1 molecules are shown in red.

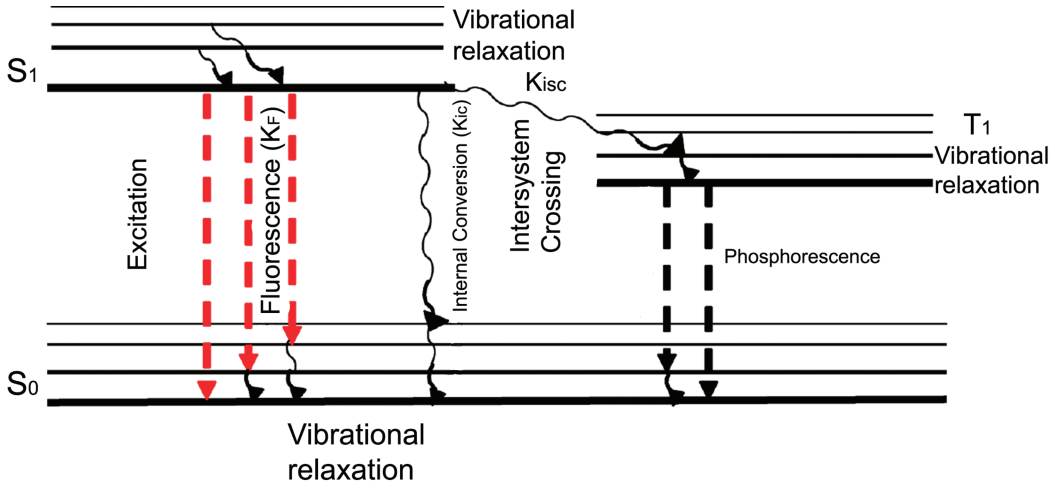

Figure 4.2. Jablonski diagram showing fluorescence decay in the presence of other radiationless, dissipative mechanisms.

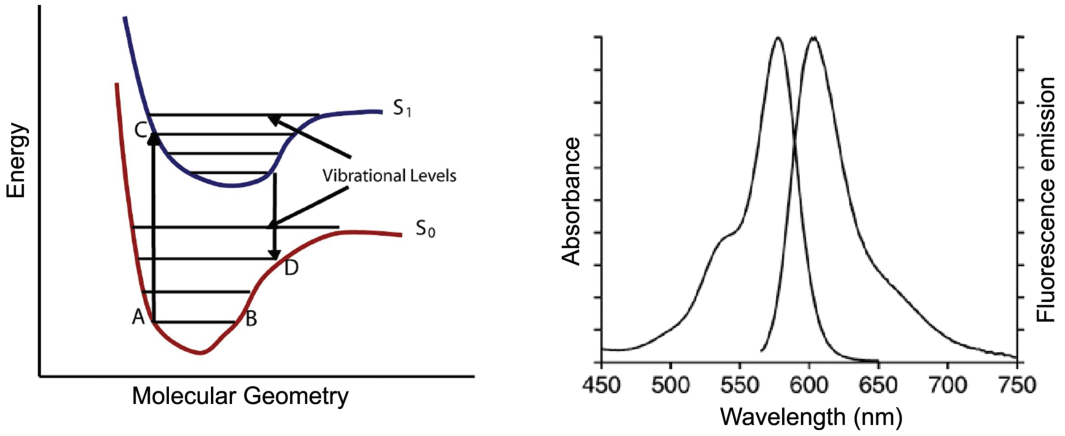

Figure 4.3. (a) Schematic representation of a molecular fluorophore with a wide range of excited- and ground-state vibration levels. (b) These are reflected in typical absorption and emission spectra.

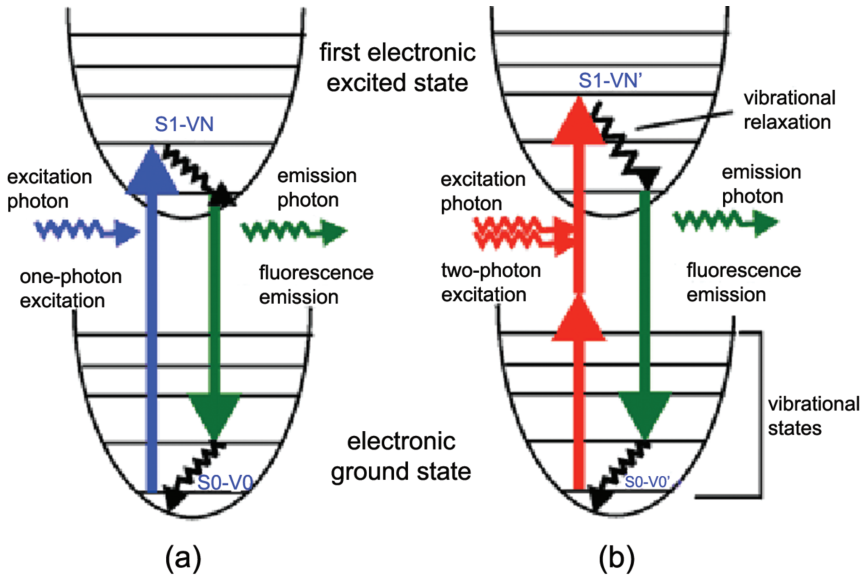

Figure 4.4. Energy-level diagram for (a) single-photon absorption fluorescence and (b) two-photon absorption fluorescence.

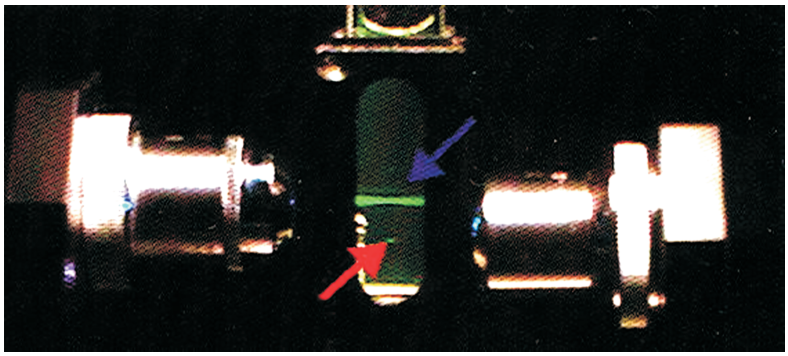

Figure 4.5. Demonstration of the z-sectioning capability of MPEF.

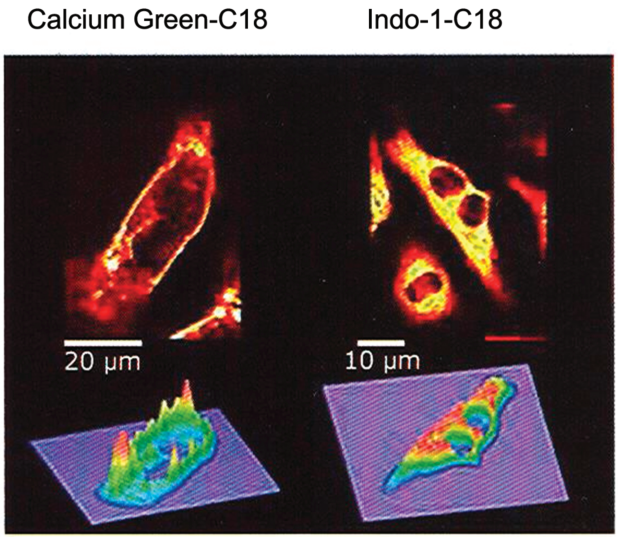

Figure 4.6. Illustration of different dyes accenting different domains of a whole cell using MPEF.

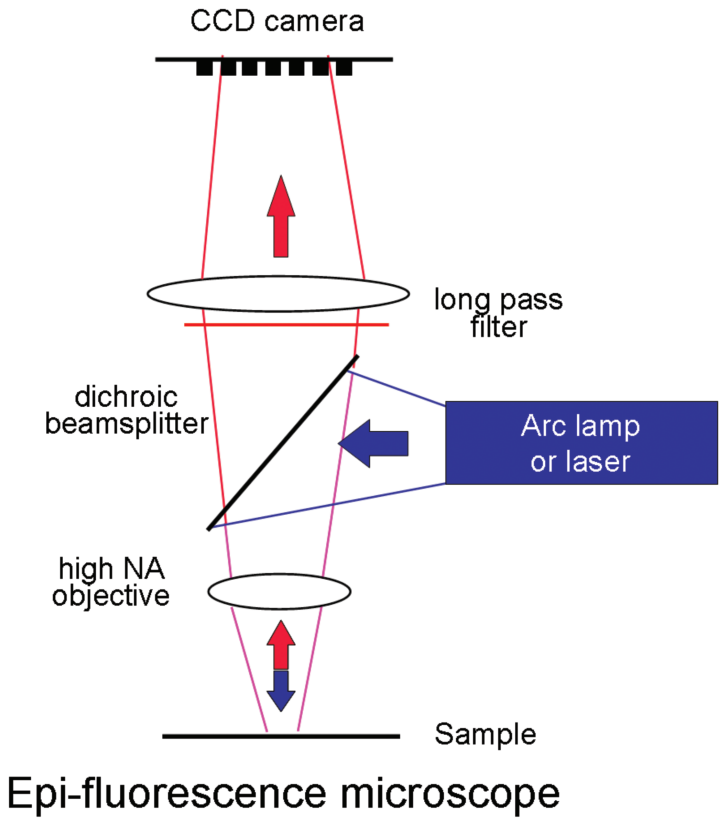

Figure 4.7. Schematic diagram for epifluorescence microscopy.

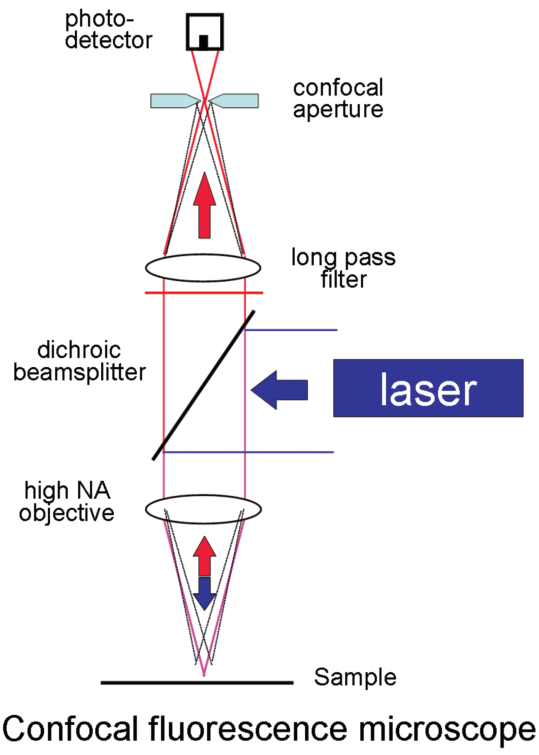

Figure 4.8. Schematic diagram of confocal microscopy geometry.

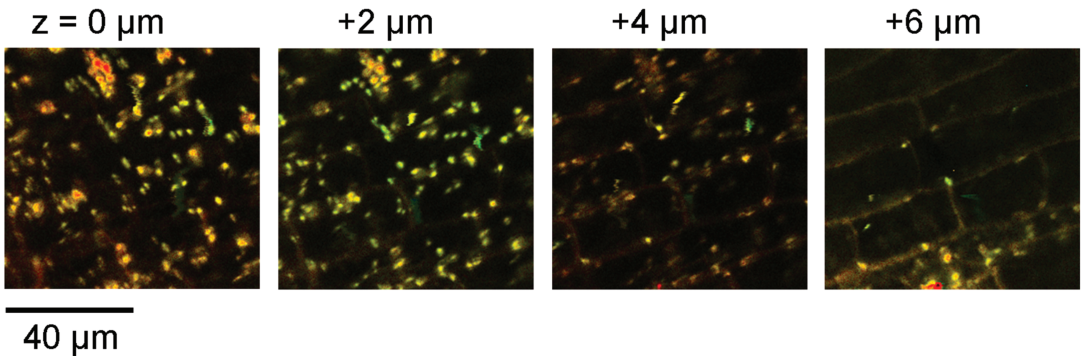

Figure 4.9. Series of two-photon confocal autofluorescence scans through the cotyledon of an *Arabidopsis thaliana* seedling from the organelle-rich interior of the plant cells (0 µm) to the cell wall (6 µm).

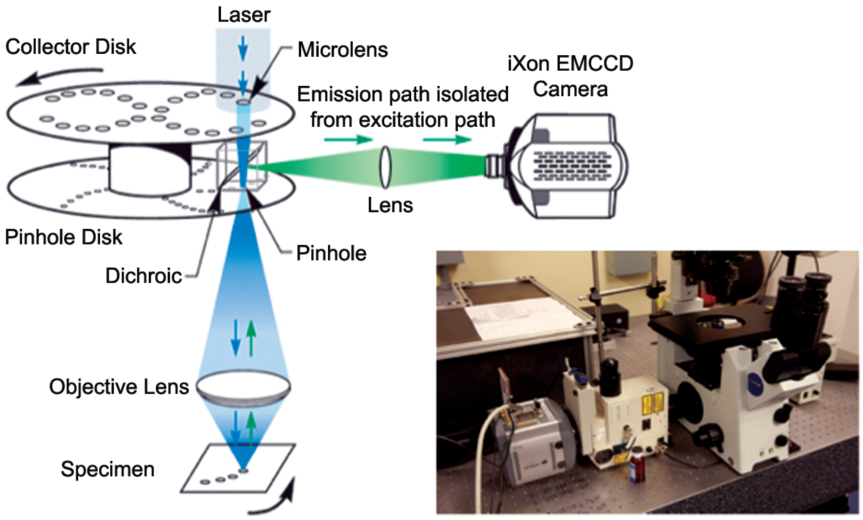

Figure 4.10. Spinning disk confocal microscopy. The multiple set of microlenses and pinholes allows simultaneous illumination of many in-focus confocal spots. Rapid spinning of this random set of pinholes leads to video-rate sampling of confocal images.

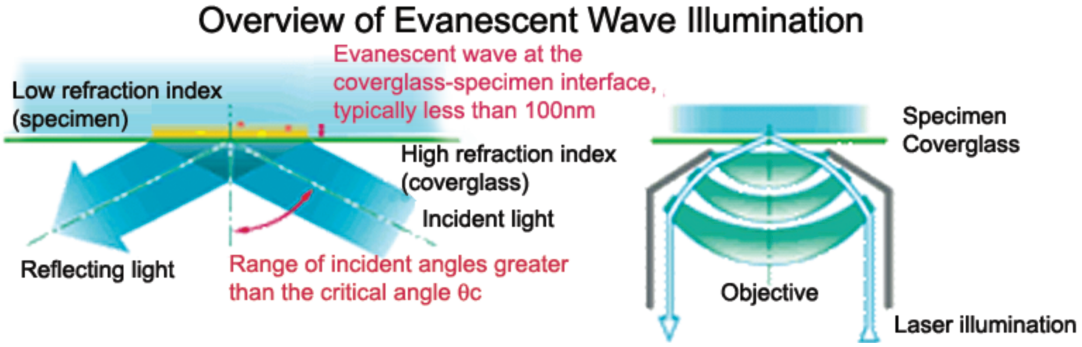

Figure 4.11. The use of total internal reflection (TIR) leads to broad-view sampling a plane within the evanescent layer, thus allowing for microscopy with considerable z-dimension discrimination.

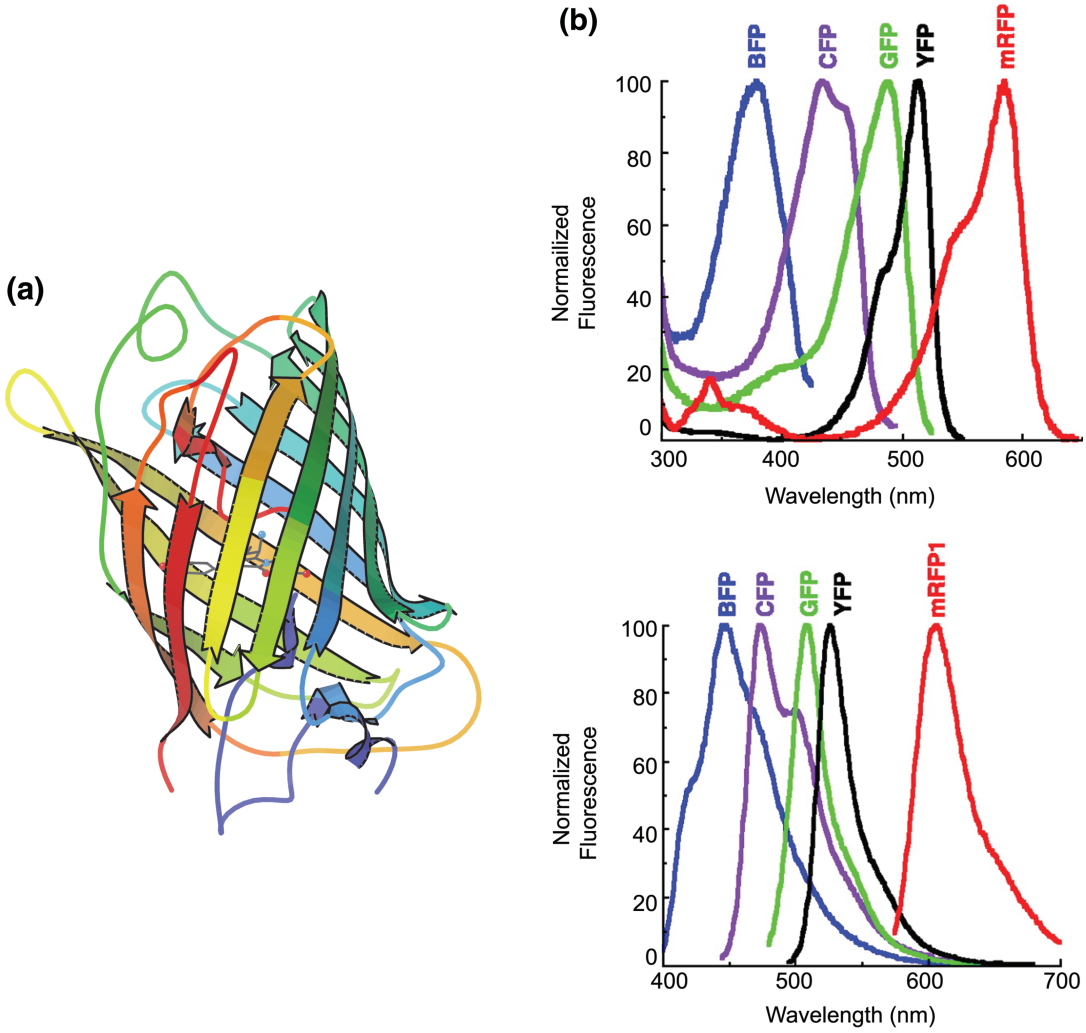

Figure 4.18. (a) Ribbon diagram of GFP in its barrel structure. Rendered from data (ID: IEMA) in the Protein Data Bank (PDB). (b) Absorption (top) and emission (bottom) spectra of variants of the GFP.

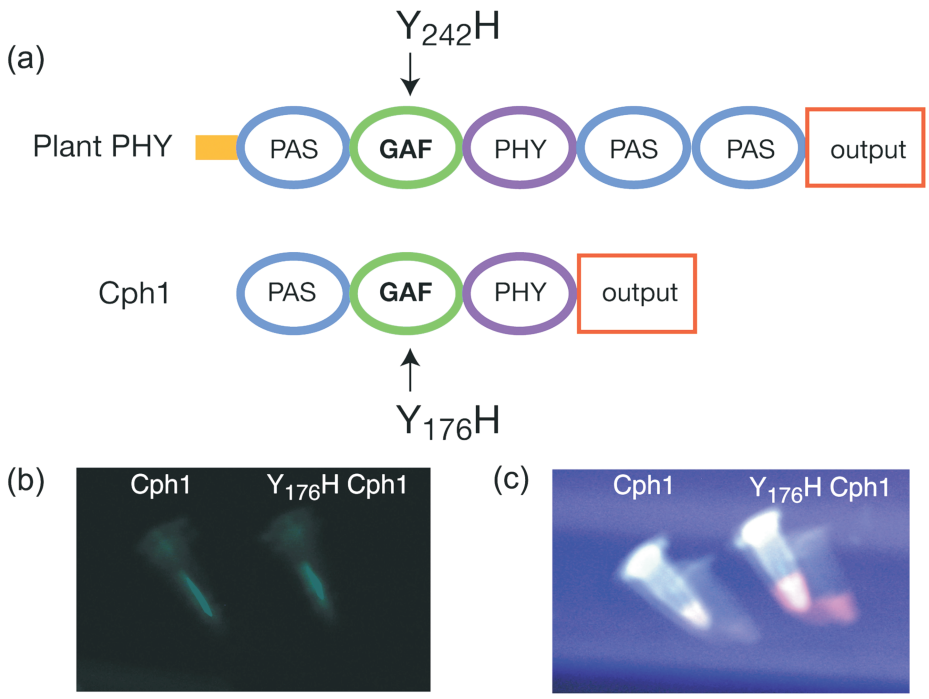

Figure 4.19. (a) Photosensitive domains exist in plant phytochromes (Plant PHY) as well as cyanobacterial phytochrome (Cph1). (b) White light illumination shows little absorption and distinction in emission between the wild type Cph1 and the mutated $Y_{176}H$ Cph1. (c) 647-nm light excitation showed that the $Y_{176}H$ mutated species are strongly fluorescent in deep red.

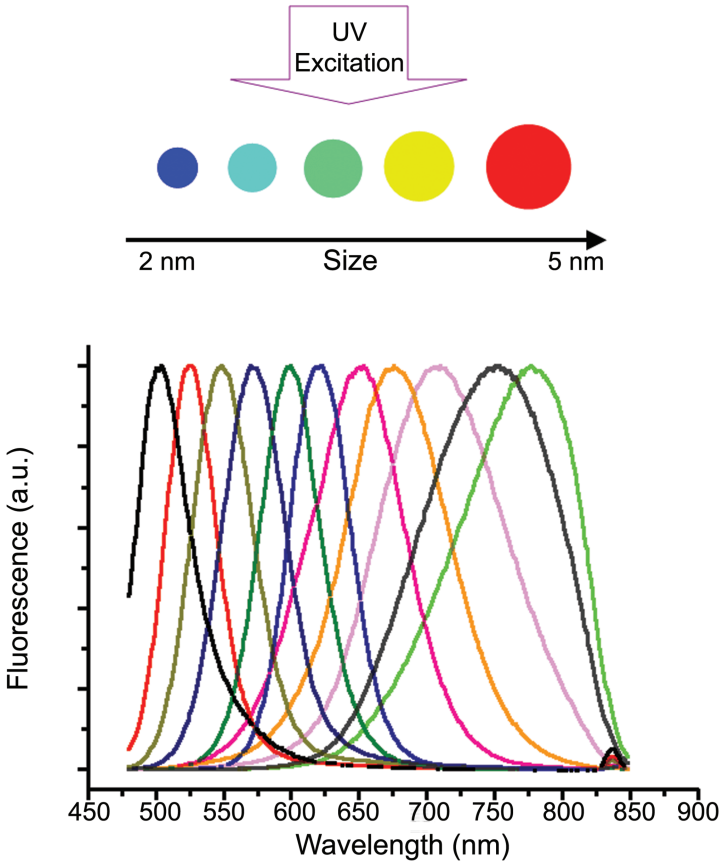

Figure 4.20. Quantum dots. Emission peak depends on the size of the quantum dots.

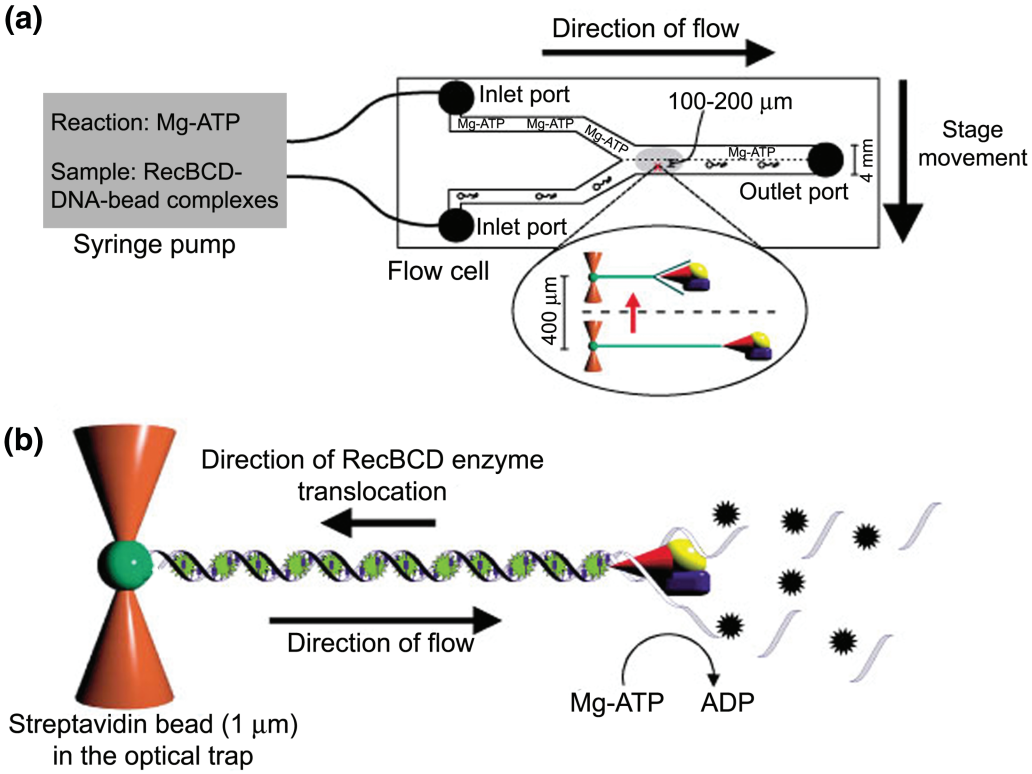

Figure 4.21. (a) Experimental design with syringe pump and flow cell. (b) Fluorescent DNA helicase assay.

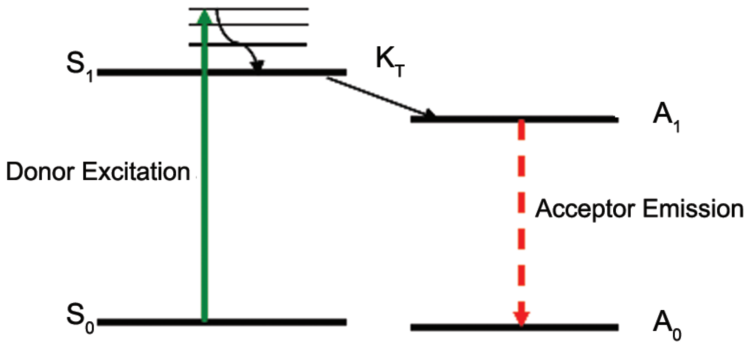

Figure 4.22. Donor and acceptor deexcitation and excitation, respectively.

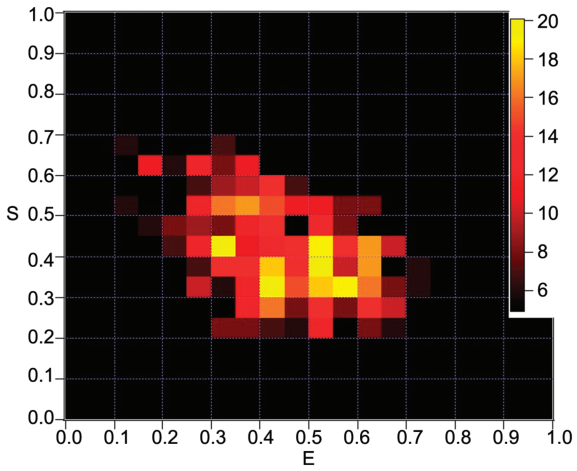

Figure 4.23. Example of a two-dimensional E–S histogram obtained with pulsed interleaved excitation FRET data acquisition.

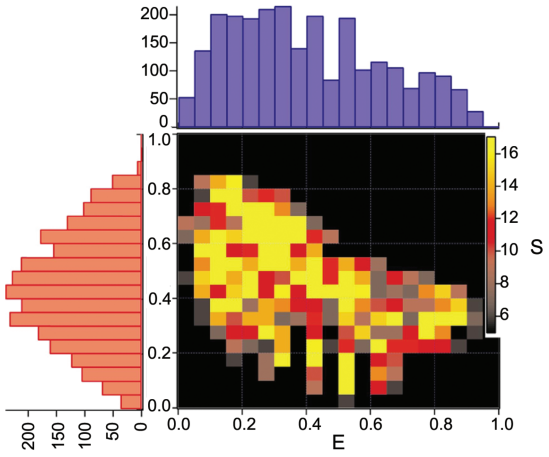

Figure 4.24. ES distribution for sample with 2 donors and 2 acceptors.

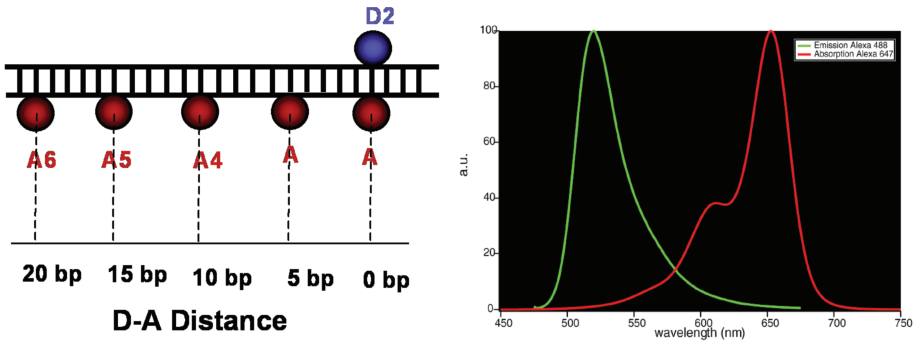

Figure 4.25. (a) Diagram of donor–acceptor distances in base pairs on DNA duplex constructs. (b) The Alexa Fluor 488 donor emission and Alexa Fluor 647 acceptor absorption.

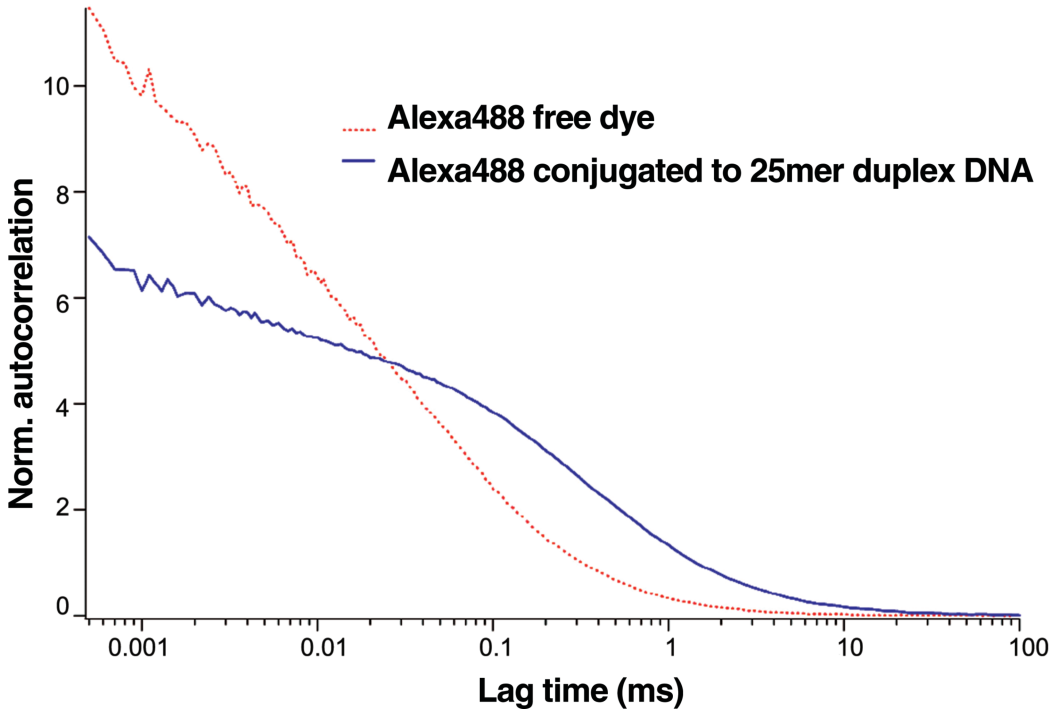

Figure 4.29. Comparison of the FCS autocorrelation calculation of Alexa Fluor 488 dye alone (red curve) and conjugated to a 25-base pair DNA duplex (blue curve).

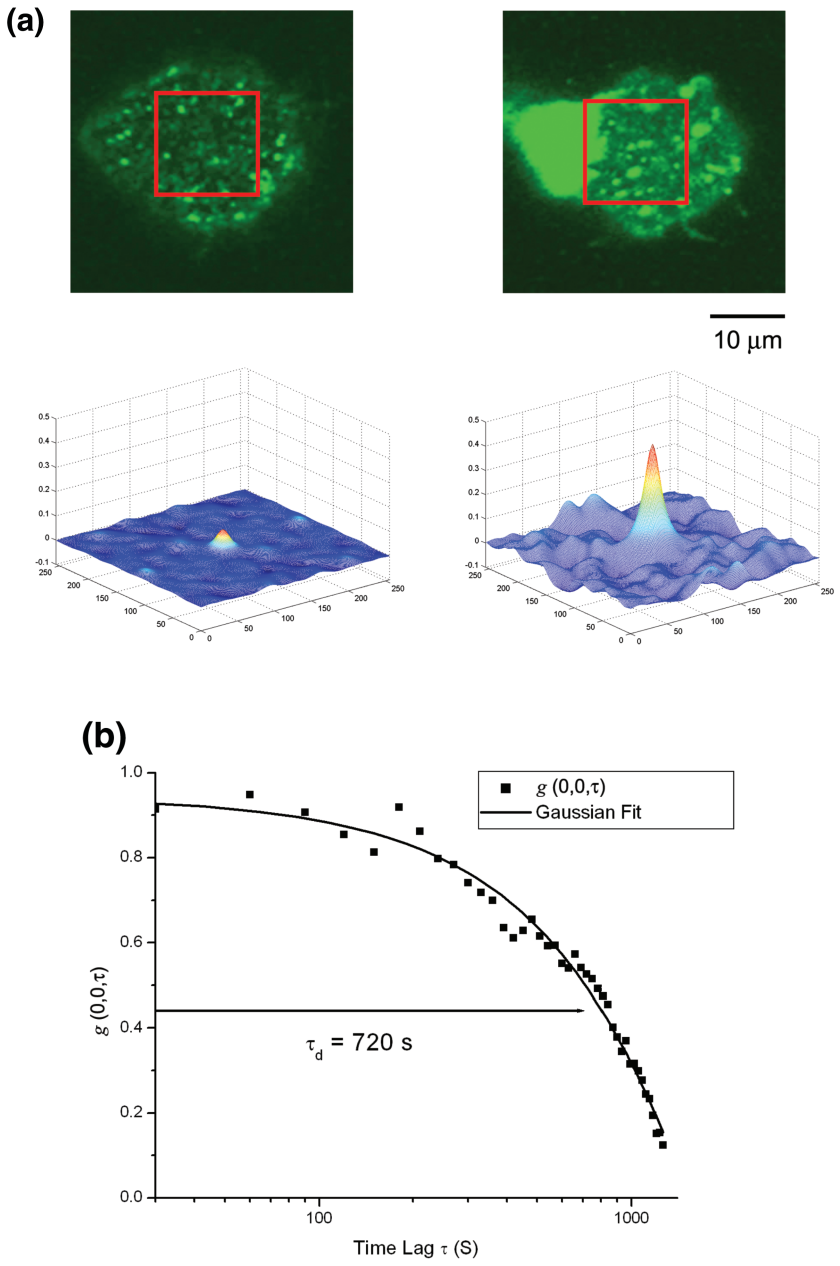

Figure 4.33. (a) Fluorescent microscopic images of healthy (*left*) and apoptotic (*right*) human retinal pigment epithelial (RPE) cells, labeled with BODIPY-FL-Gm1, and their autocorrelation functions (spatial I-FCS) of cropped areas. (b) Cross-correlation (temporal I-FCS) function $g_{ij}(0,0,\tau)$ computed from a sequence of images of healthy RPE cells, taken every 30 seconds.

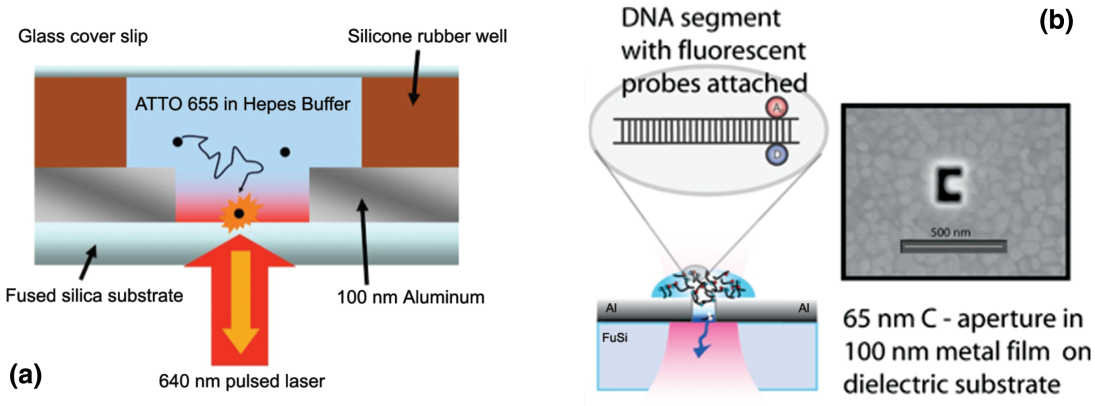

Figure 4.34. (a) Concept of a zero-mode waveguide-illuminated fluorescence event. (b) Special naonpore is shaped in the for a the letter "C."

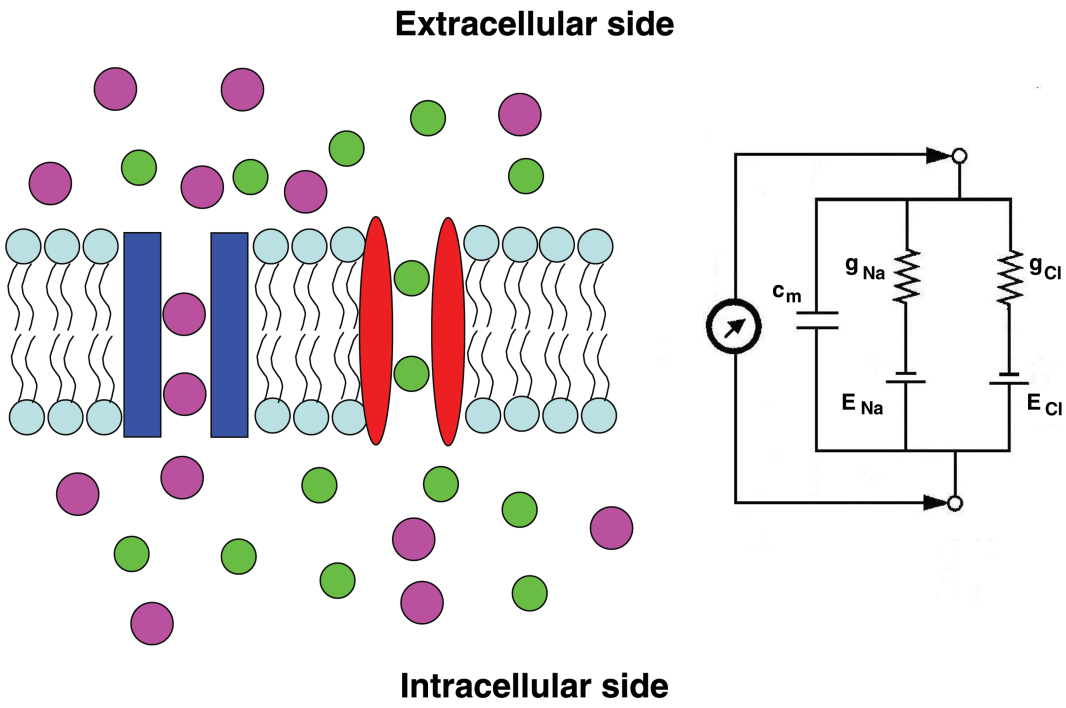

Figure 5.1. Equivalent electrical circuit for membrane current.

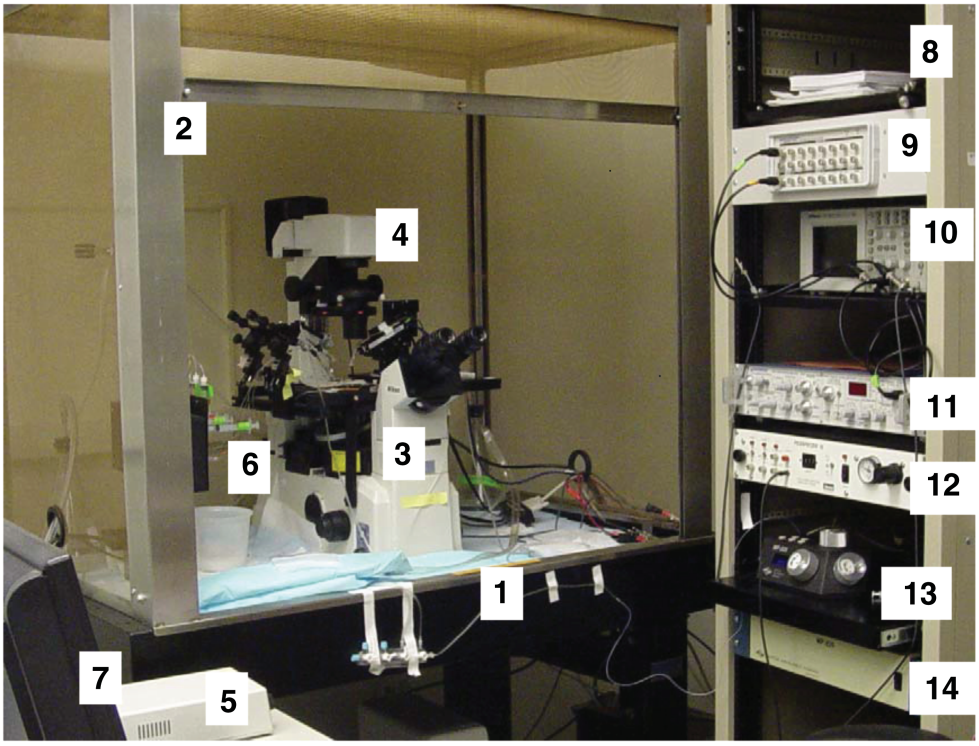

Figure 5.6. A patch-clamp setup.

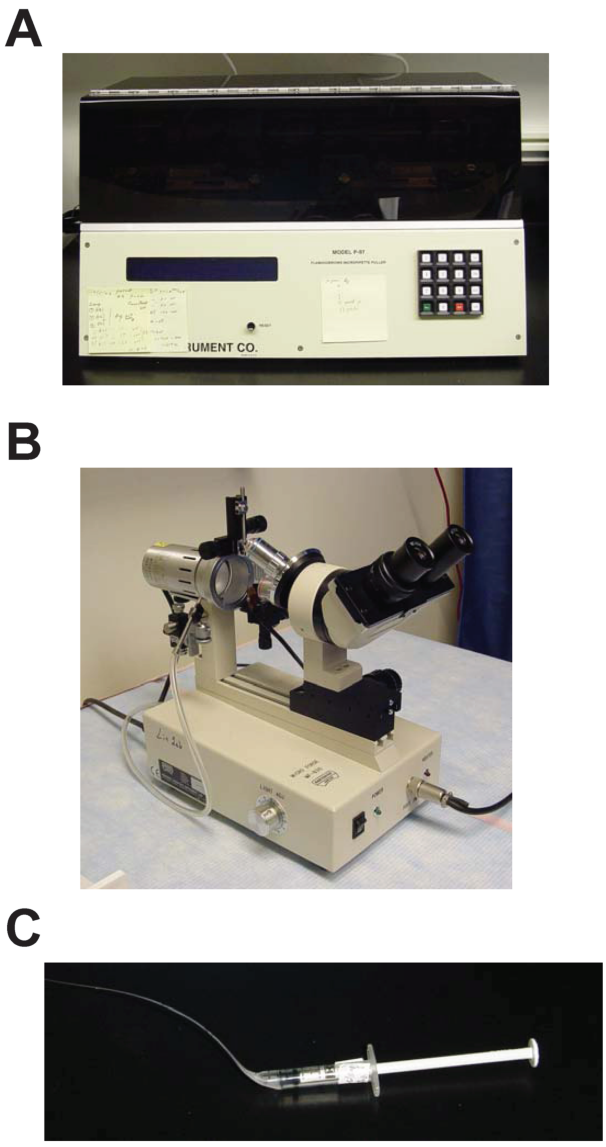

Figure 5.7. Devices for fabrication and filling of glass recording electrodes.

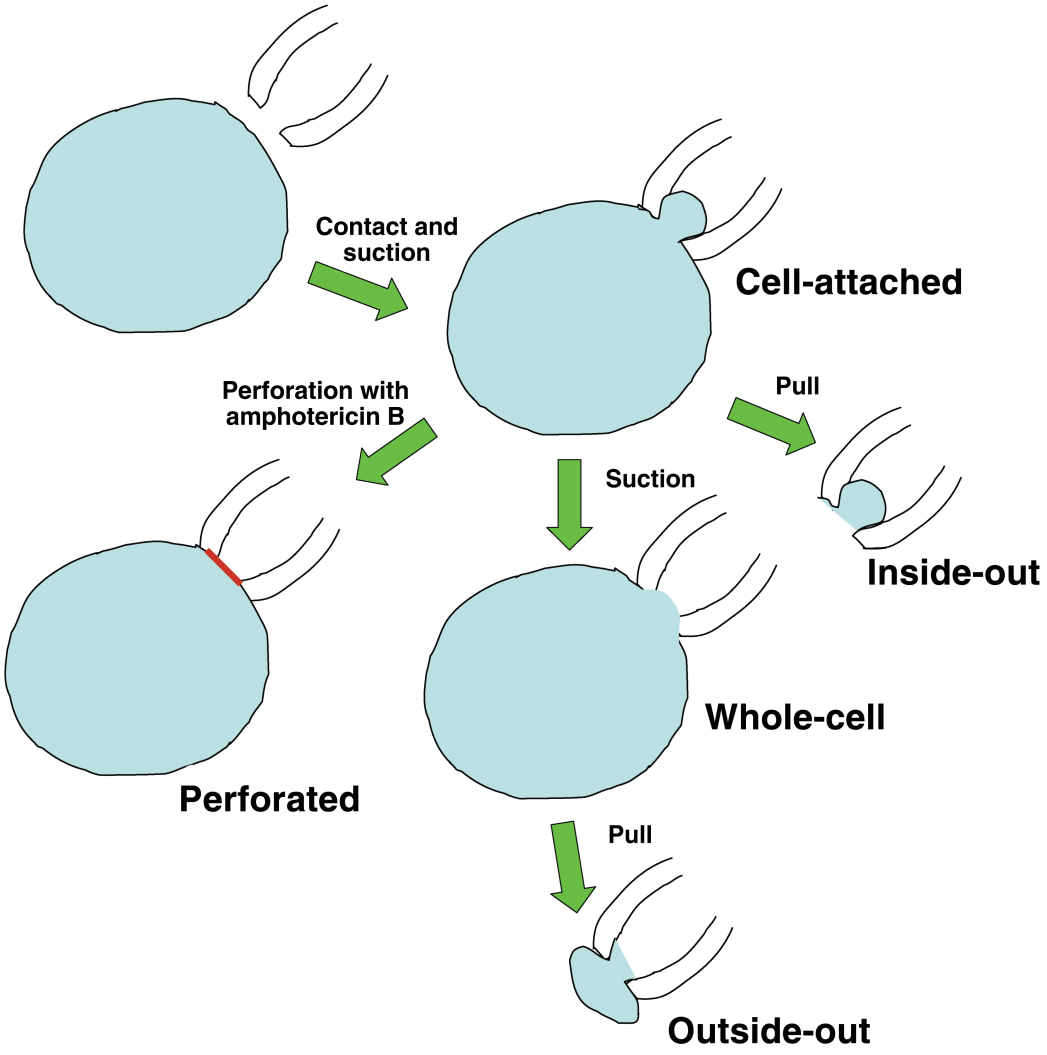

Figure 5.8. Schematic diagrams of different configurations of patch-clamp recordings.

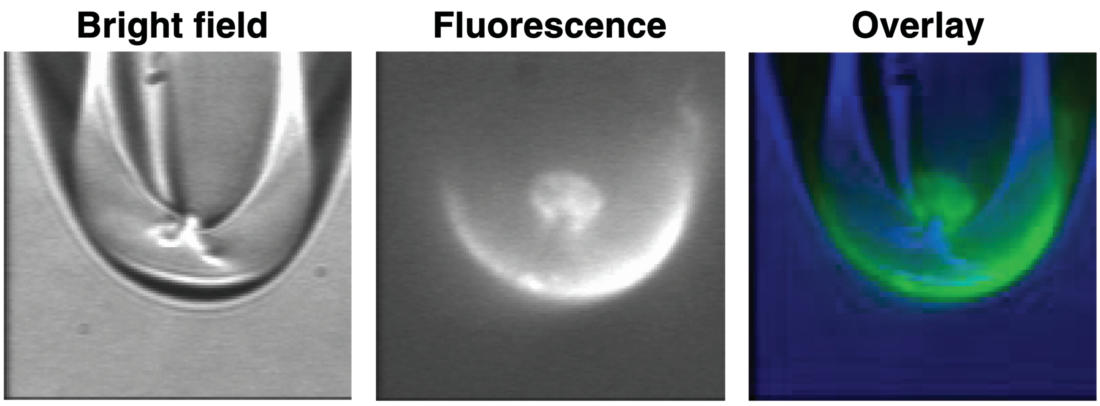

Figure 5.11. Patch-clamp fluorometry.

http://www.springer.com/978-1-58829-973-4

Fundamental Concepts in Biophysics
Volume 1
Jue, Th. (Ed.)
2009, VIII, 248 p. 9 illus., 7 illus. in color., Hardcover
ISBN: 978-1-58829-973-4
A product of Humana Press